Single Copper Atoms Enhance Photoconductivity in

$g-C_3N_4$

Matt D. Capobianco,† Brian Pattengale,†,* Jens Neu,‡,* Charles A. Schmuttenmaer†,§

†Department of Chemistry and Yale Energy Sciences Institute, Yale University, New Haven,

Connecticut 06520-8107, United States

[‡]Department of Molecular Biophysics and Biochemistry and Yale Microbial Sciences Institute,

Yale University, New Haven, Connecticut 06520-8107

§Deceased July 26, 2020

AUTHOR INFORMATION

Corresponding Author

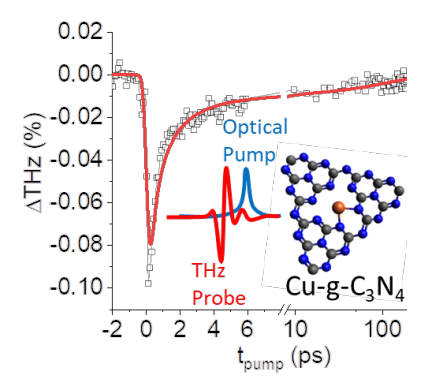
*Brian Pattengale; brian.pattengale@yale.edu

*Jens Neu; jens.neu@yale.edu

ABSTRACT

Graphitic carbon nitride (g- C_3N_4) and its doped analogues have been studied over the past decade in part due to their promising applications in heterogeneous photocatalysis, however, the effect of doping on the photoconductivity is poorly understood. Herein, we investigate Cu doped g- C_3N_4 (Cu-g- C_3N_4) and demonstrate via EXAFS that Cu⁺ incorporates as an individual ion. Time-resolved optical pump terahertz probe (OPTP) spectroscopy was utilized to measure the ultrafast photoconductivity in response to a 400 nm pump pulse and showed that the Cu⁺ dopant significantly enhances photoconductivity of the as-prepared powdered sample, which decays within 10 ps. Furthermore, a film preparation technique was applied that further enhanced the photoconductivity and induced a longer-lived photoconductive state with a lifetime on the order of 100 ps. This study provides valuable insight into the ultrafast photoconductivity dynamics of g- C_3N_4 materials, which is essential toward developing efficient g- C_3N_4 photocatalysts.

TOC GRAPHICS



KEYWORDS 2D Materials, Terahertz Spectroscopy, Ultrafast Spectroscopy, Materials Physics, Photocatalysis, X-ray Absorption.

Graphitic carbon nitride (g-C₃N₄) is a 2D semiconductor that is of intense interest to the field of photocatalysis due to its earth abundant elemental composition, stability, and numerous applications, further complemented by a high degree of tunability with respect to modifications that alter its light absorption and catalytic efficacy. 1-6 The unmodified material has a bandgap of 2.6 eV (corresponding to an absorption wavelength of 477 nm) and band positions appropriate for both half reactions of water splitting.^{3,7} It has been used for the hydrogen evolution reaction,^{3,7} photodegradation,^{4,8-10} and other reactions including CO₂ reduction⁷ and transformations.^{11,12} Elemental doping has been widely applied to engineer the bandgap and improve the photocatalytic efficacy of g-C₃N₄ in these classes of photocatalytic reactions.^{5,13-17} Having advantages of high earth abundance and environmental friendliness, copper doping is commonly used to enhance the photocatalytic performance of g-C₃N₄.6,13,18-20 Despite these promising applications in photocatalysis, understanding of the photon-initiated dynamics in g-C₃N₄ and its doped analogues, as they relate to photocatalytic performance, remains elusive. Particularly, the photoconductivity, which is the property that directly affects the migration of photogenerated carriers to catalytically active sites, has not been thoroughly investigated on the femtosecond-picosecond timescales relevant to carrier dynamics.²¹⁻²⁵

Due to its subpicosecond time resolution, sensitivity to mobile charge carriers, and applicability to emerging classes of materials such as 2D materials and metal-organic frameworks, ²⁶⁻³⁰ optical pump terahertz (THz) probe spectroscopy (OPTP) is an excellent tool to probe the photoconductivity of bulk g-C₃N₄ in a contact-free manner. THz radiation is absorbed by mobile carriers and its absorption is proportional to the product of their free carrier density and mobility. Dynamic photoconductivity information such as the onset of photoconductivity, carrier

trapping, and recombination is gained by monitoring the change in THz transmission as a function of delay of the excitation pulse.³¹⁻³³

In this work, we investigate a promising photocatalyst material, g-C₃N₄ doped with Cu (Cug-C₃N₄), alongside its undoped analogue. Using extended X-ray absorption fine structure (EXAFS), we unambiguously demonstrate that the synthetic methods employed yield single-atom Cu⁺ sites anchored to the 2D layers of g-C₃N₄. The dopant modifies the UV-Visible absorption and emission properties of the material. Via OPTP, we correlate these properties with the photoconductivity dynamics and demonstrate that the single Cu atoms provide significant photoconductivity improvement to g-C₃N₄. In addition to studying the bulk material, we demonstrate that film fabrication methods employed have an even larger effect on the photoconductivity and result in an increase of at least two orders of magnitude in the carrier lifetime as well as more than doubling the magnitude of the photoconductivity in Cu-g-C₃N₄. These results indicate that valuable information can be obtained by using OPTP to study g-C₃N₄ materials relevant to photocatalysis, thereby providing understanding and insight into improving their photoconductivity.

Undoped g-C₃N₄ and Cu-g-C₃N₄ were prepared according to a previously published procedure employing dicyandiamide, with the addition of CuCl₂•2H₂O to synthesize the doped sample.¹³ The synthetic methods employed are reported to give the desired 2D g-C₃N₄ product composed of repeating tri-s-triazine units.^{13,34,35} The XRD pattern (Figure 1a) shows the expected primary diffraction feature at $2\theta = 27.35^{\circ}$ that is reported as the (002) plane and corresponds to an interlayer distance of 3.35 Å.^{3,35} The diffraction observed at $2\theta = 13.0^{\circ}$ is in agreement with previous reports and assigned to an intralayer diffraction. The diffraction peak positions observed

in both g-C₃N₄ and Cu-g-C₃N₄ are consistent with a structure composed of repeating tri-s-triazine units, suggesting that Cu incorporation does not alter the bulk structure of the material.³⁵ The pXRD peaks were fit using a Lorentzian function (Figure 1a, inset and Table S1) yielding the result that Cu-doping reduces the interlayer distance by approximately 0.02 Å and also reduces the peak FWHM by nearly 20%. This work also employed a strategy to prepare sintered films of g-C₃N₄ and Cu-g-C₃N₄ using the methods of Ito et al.,³⁶ which are more relevant to photoelectrochemical devices than a bulk powder. High-quality films are obtained (Figure S1) and the XRD results and fitting analysis (Figure S2 and Table S1) show the main diffraction feature is shifted significantly to $2\theta = 27.68^{\circ}$ and $2\theta = 27.62^{\circ}$ revealing a shortened interlayer distance due to film preparation and reduction in the peak FWHM on the order of 20% compared to g-C₃N₄ powder. Therefore, Cudoping of g-C₃N₄ results in closer and more homogeneous stacking of the 2D sheets, and film preparation has a similar effect.

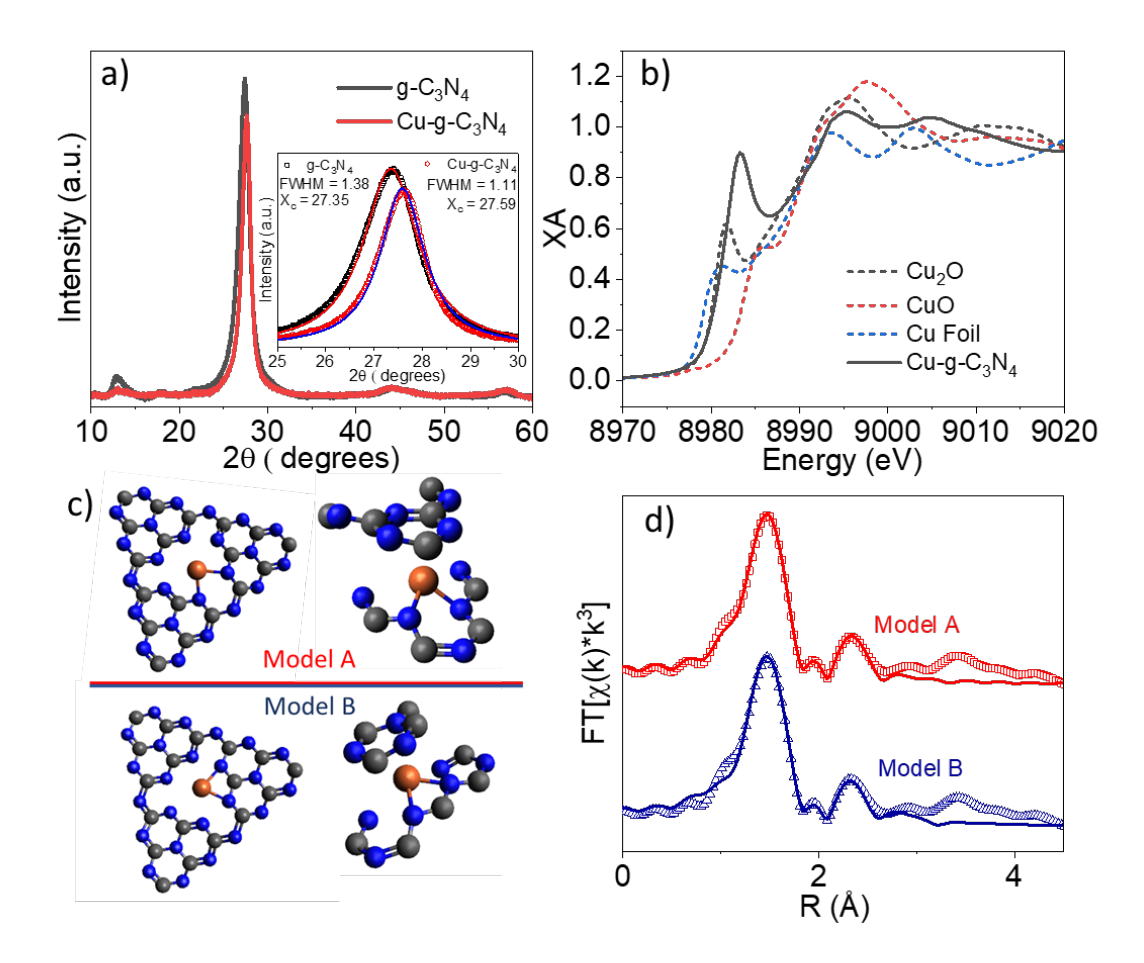


Figure 1. (a) XRD patterns of g-C₃N₄ and Cu-g-C₃N₄ powders. Inset: Enlarged region of main XRD feature and Lorentzian best fits. (b) XANES spectra at the Cu K edge for Cu-g-C₃N₄ (solid line) and references (dashed lines). (c) The two proposed EXAFS models fit in this work, with the left structure showing the anchoring of the Cu dopant to a single sheet and the right structure showing the fit model, including nearby atoms from the sheet above. (d) R-space EXAFS spectra and FEFF best fit lines for each fit model.

The local structure of the Cu dopant was investigated using X-ray absorption spectroscopy. Using this technique, the X-ray absorption near edge structure (XANES) region can give insight into the electronic structure and oxidation state of the probed atom and the extended X-ray

absorption fine structure (EXAFS) region can be analyzed to determine both the number of photoelectron scattering interactions (interpreted as coordination number, *N*, in the first shell) and interatomic distances, *R*, thereby providing insight into the electronic and local structure. The Cu K edge XANES spectra of Cu-g-C₃N₄ and reference samples are shown in Figure 1b. All spectra show a strong feature on the rising edge corresponding to a dipole-allowed transition from 1s to a partially bound state with significant 4p character.³⁷ Absorption beyond this feature is also associated with a 1s-4p transition into a continuum state. In the reference spectra, the position of the peak and the absorption edge is observed to be highly dependent on oxidation state. The edge positions were quantified (Figure S3a and Table S2) demonstrating the edge position of Cu-g-C₃N₄ to be close to that of the Cu⁺ reference, and we therefore assign the oxidation state of the Cu dopant as Cu⁺. Cu-g-C₃N₄ was measured alongside CuO and Cu₂O references in XPS measurements, further confirming the oxidation state as Cu⁺ in both Cu-g-C₃N₄ powder and film samples (Figure S4).

Table 1. EXAFS best fit results for Cu-g-C₃N₄. Fit uncertainties given in parentheses and fixed quantities denoted with an asterisk. N is the vector number, interpreted as coordination number in the first shell, σ^2 is the Debye-Waller factor accounting for static and dynamic disorder, ΔE_0 is the phase shift of the fit, and R is the fit vector distance, or interatomic distance for single scattering events.

Model	Vector	N^*	$\mathbf{\sigma}^{2}$ ($\mathbf{\mathring{A}}^{2}$)	$\Delta E_0 (eV)^*$	R (Å)
Model A	Cu - N	2	0.005(5)	-2.35	1.916(4)
	Cu - C	1	0.011(4)	-4.89	2.46(2)
	Cu - N	2	0.009(5)	-4.89	2.65(2)
	Cu - C	1	0.001*	-4.89	2.81(3)
Model B	Cu - N	2	0.0045(1)	4.71	1.92(1)
	Cu - C	1	0.005^{*}	-8.24	2.04(3)
	Cu - N	2	0.004(1)	-4.66	2.78(1)
	Cu-N-C	4	0.002^{*}	-4.66	2.81(5)

The intensity of the bound state 1s-4p transition observed on the edge is significantly more intense for Cu-g-C₃N₄ than the transitions observed in the reference data. Low-coordinate Cu⁺ species have been reported to display an intense feature on the edge due the splitting of the $4p_{x,y,z}$ molecular orbitals resulting in the observation of a 1s-4p_{x,y} transition on the edge separate from the transition to the antibonding 4p_z orbital.³⁷ A preliminary EXAFS analysis found that the first shell scattering was best represented by two nearest neighbors at approximately 1.9 Å. Given this preliminary analysis, two potential models could be constructed (Figure 1c) based on the reported X-ray crystal structure.³⁸ The models we constructed independently are also in agreement with a literature report.²⁰ The quantitative EXAFS results are displayed in Table 1 and the fits are shown in R-space (Figure 1d) and K-space (Figure S5). The second shell interactions observed in Cu-g-C₃N₄ agree well with scattering interactions with surrounding C or N atoms. In comparison, the reference CuO and Cu₂O R-space spectra (Figure S3b) show intense second shell features at a longer distance and those features are dominated by Cu-Cu scattering. Despite its low coordination number (N) of 2, the Cu atoms in Cu-g- C_3N_4 evidently do not have any neighboring atoms besides small C and N atoms in the 2D g-C₃N₄ layers. Therefore, while neither model A nor B can be definitively assigned, the EXAFS results demonstrate that Cu atoms in Cu-g-C₃N₄ are best described as low-coordinate single Cu⁺ atoms anchored to the 2D layers of g-C₃N₄.

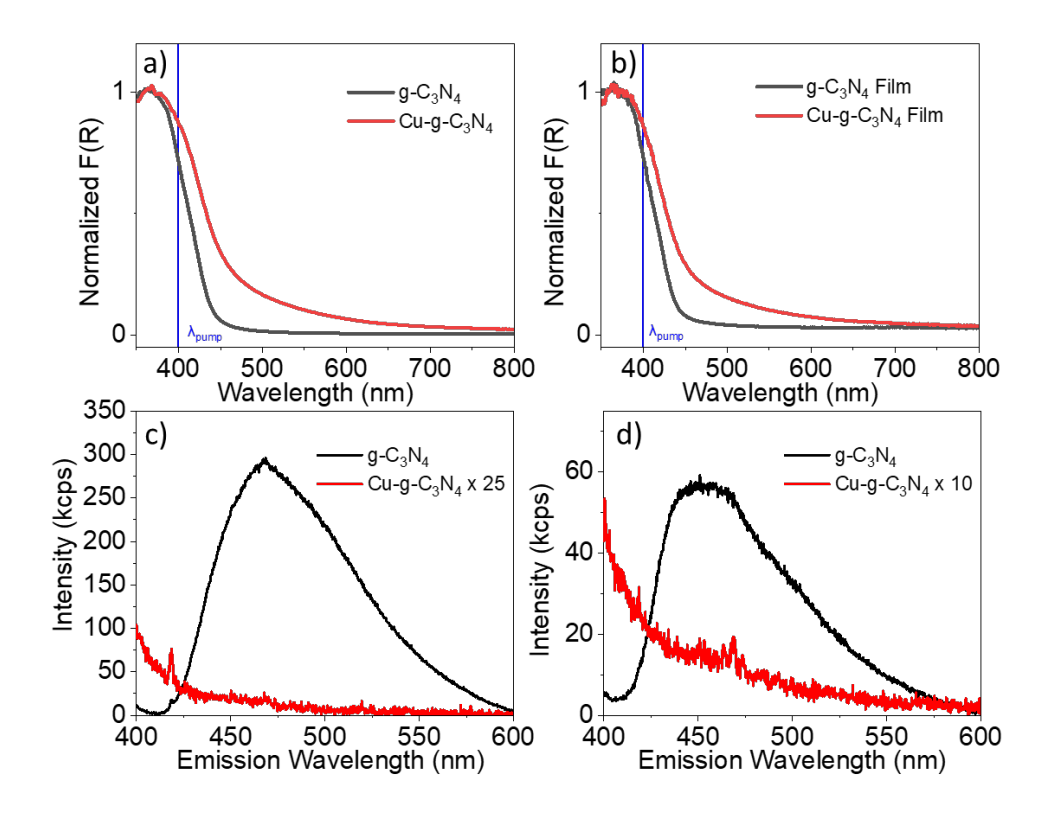


Figure 2. (a) Kubelka-Munk transformed diffuse reflectance UV-Visible spectra for powder samples and (b) film samples on quartz. Emission spectra of (c) powder and (d) film samples on quartz under 380 nm excitation. Cu-g-C₃N₄ emission spectra enlarged in (c-d) to show absence of signal above the noise.

The UV-Visible spectra (Figure 2a,b) were measured in diffuse reflectance mode and transformed via the Kubelka-Munk function as described in the SI. The powder (Figure 2a) and film (Figure 2b) samples show nearly identical spectra. Tauc plots (Figure S6) determine a bandgap of approximately 2.65 eV for undoped g-C₃N₄ whereas Cu-g-C₃N₄ has a smaller bandgap and shows additional absorption throughout the visible region of the spectrum. Because Cu⁺ is typically d¹⁰, it is unlikely that the additional transitions observed in the visible region are due to transitions within the Cu d-manifold, suggesting that they involve an interaction with g-C₃N₄. The

emission spectrum of g-C₃N₄ powder is shown in Figure 2c where it is also shown that Cu-doping fully quenches the emission after 380 nm above-bandgap excitation. Film g-C₃N₄ (Figure 2d) shows a different fluorescence line-shape and blue-shifted peak position (comparison in Figure S7). In support of this result, previous reports have shown that the fluorescence spectrum is composed of multiple components that each vary in intensity due to synthetic/processing conditions, resulting in shifting of the fluorescence maximum.³⁹⁻⁴¹ Full quenching due to Cu doping is also observed in film samples (Figure 2d). Steady-state fluorescence quenching in doped g-C₃N₄ systems has been previously explained to be due to charge transfer after bandgap excitation of g-C₃N₄.^{15,42,43} Charge transfer transitions in the UV-Visible absorption spectra have been reported and suggested to be metal-to-ligand charge transfer (MLCT) in nature in g-C₃N₄ analogues containing a Cu species^{6,44} or Pt species.^{6,45} A recent computational study reproduced the change in bandgap and visible light absorption in Cu-g-C₃N₄ compared to g-C₃N₄ and further found photoinduced electron depletion at Cu due to MLCT.⁴⁶ Therefore, we conclude that a charge transfer state exists below the bandgap in Cu-g-C₃N₄ wherein low-valent Cu⁺ transfers charge to g-C₃N₄, which should result in enhanced carrier density in g-C₃N₄ and, therefore, enhanced photoconductivity if those carriers are mobile (i.e. not trapped).

We investigated the photoconductivity of g-C₃N₄ and Cu-g-C₃N₄ using optical pump terahertz probe spectroscopy (OPTP) as described in the Experimental Methods section (SI) and Figure S8. The data was collected by monitoring the attenuation of the peak of the THz wave as a function of pump time delay. Photoinduced attenuation of the THz pulse is a result of mobile carriers being generated in the sample.^{32,47} The decay of the transient attenuation provides information on trapping and/or recombination processes. Bulk powder samples without any further

treatments were measured using the "tape cell" method described in the Experimental Section, and the film samples on fused quartz were measured directly.^{31,48-50}

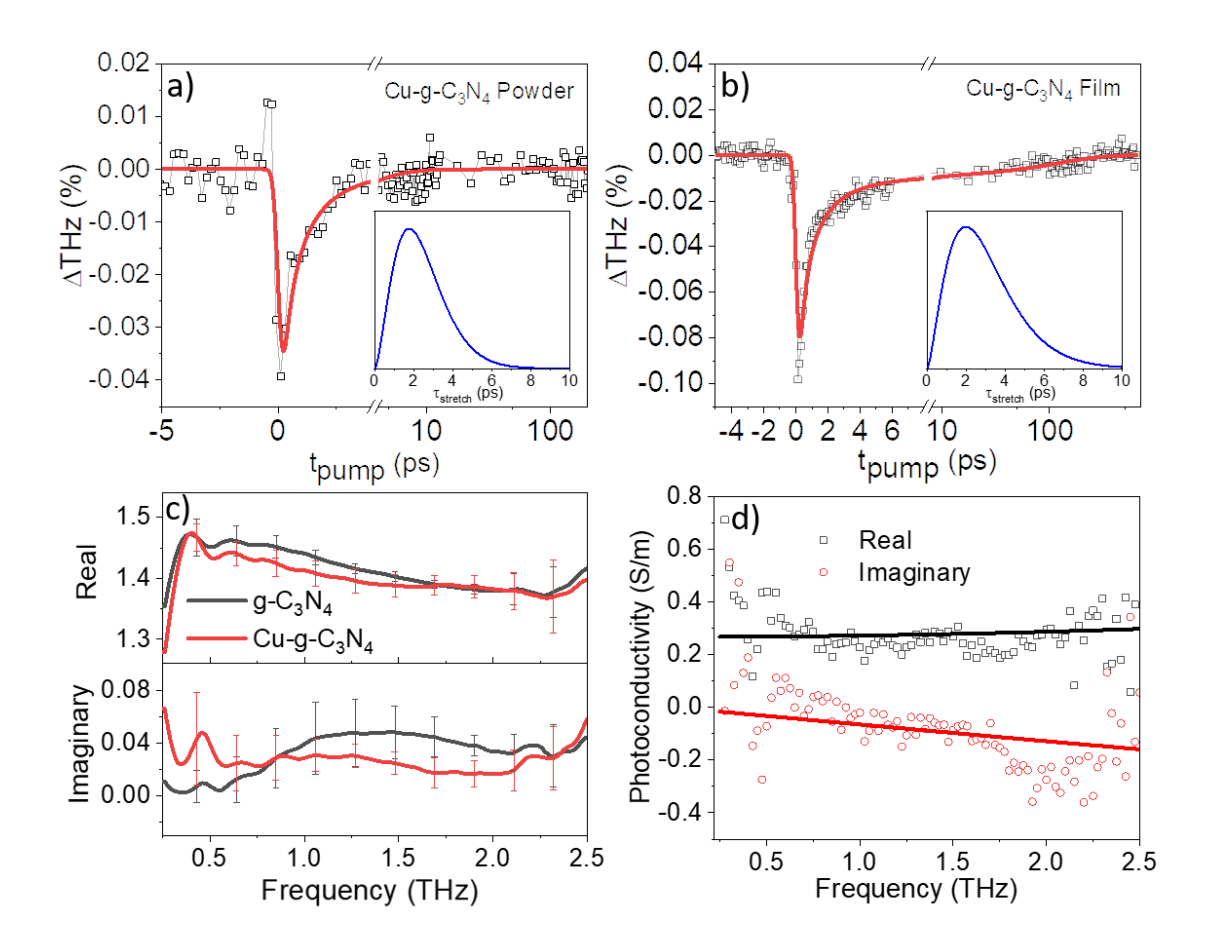


Figure 3. OPTP traces for (a) Cu-g-C₃N₄ powder and (b) Cu-g-C₃N₄ film. The data is shown as open points and the fits as solid lines. Insets show the calculated distributions of the stretched time constant. (c) THz-TDS spectra comparing g-C₃N₄ and Cu-g-C₃N₄ film samples. (d) TRTS spectrum for Cu-g-C₃N₄ film with Drude-Smith fit as solid lines.

OPTP results have not been published for $g-C_3N_4$ previously. In the materials prepared for this study, undoped $g-C_3N_4$ powder consistently does not yield measurable signal (Figure S9a). In

contrast, Cu-g-C₃N₄ powder yields a clearly observable OPTP transient (Figure 3a). Thus, it is seen that the presence of isolated Cu⁺ ions in the material dramatically enhances the photoconductivity. Taking the materials a step closer toward photocatalytic device applications, films were prepared utilizing the preparation of Ito et al via doctor blading.³⁶ For Cu-g-C₃N₄ film (Figure 3b), the magnitude of the peak THz attenuation is nearly double that of the powder, suggesting that the film preparation methods further enhance the photoconductivity. In addition, the film preparation procedure results in measurable photoconductivity for the undoped g-C₃N₄ film (Figure S9b).

In comparing the Cu-g- C_3N_4 film data to the Cu-g- C_3N_4 powder data, it is also observed that the film preparation results in a long-lived OPTP component not observed in the powder. This component is also observed in the undoped g- C_3N_4 film data (Figure S9b). These qualitative observations were quantified by fitting the OPTP decay to the models shown below:

$$-\Delta T H z = \left[A_{stretch} e^{\left(-\frac{(t_{pump} - t_0)}{\tau_{stretch}}\right)^{\beta}} \right] \otimes G_R(fwhm)$$
 (1)

$$-\Delta T H z = \left[A_{stretch} e^{\left(-\frac{(tpump-t_0)}{\tau_{stretch}}\right)^{\beta}} + A_2 e^{\left(-\frac{tpump-t_0}{\tau_2}\right)} \right] \otimes G_R(fwhm)$$
 (2)

$$\langle \tau \rangle = \frac{\tau}{\beta} \Gamma \left(\frac{1}{\beta} \right) \tag{3}$$

Table 2. Fit Parameters for OPTP traces using Equations 1 and 2.

Sample	$G_R(ps)$	$A_{stretch}$	$ au_{stretch}$ (ps)	β	A_2	τ_2 (ps)
Cu-g-C ₃ N ₄ powder	0.4	-0.074	0.45	0.57		
Cu - g - C_3N_4 film	0.4	-0.16	0.40	0.53	-0.009	119

Cu-g-C₃N₄ powder data was fit using a single stretched exponential function (Equation 1) to account for the heterogeneity in trapping and recombination processes that result in the decay of the OPTP transient.31,33 The best fit results are shown in Table 2, where A represents the amplitude of the exponential, τ represents the lifetime, and G_R represents the fwhm of the Gaussian instrument response function (IRF), and \otimes represents the convolution of the IRF with the fit function. The stretched time constant ($\tau_{stretch}$) for Cu-g-C₃N₄ powder fit to 0.45 ps with a β value of 0.57. Using these parameters, the expectation value of the lifetime distribution can be determined via Equation 3 as 0.80 ps. The Cu-g-C₃N₄ film, due to its longer lifetime, required an additional non-stretched component as shown in Equation 2. The stretched component, $\tau_{stretch}$, fit to 0.40 ps with a β value of 0.53 yielding a mean stretched lifetime of 0.82 ps. This mean lifetime is in close agreement with that of the powder Cu-g-C₃N₄ sample, implying that while the magnitude of photoconductivity is larger in the film, the dynamics are similar in the subpicosecond time regime. The distributions of the stretched time constants are shown in the insets of Figures 3a-b and were calculated using the methods reported by Elton.⁵¹ At longer delay times, however, Cu-g-C₃N₄ film fit with a τ_2 value of 119 ps and this component was not present in the powder. Furthermore, the undoped g-C₃N₄ film data (Figure S9b) could be adequately described with Equation 2 and yielded a τ_2 value of 41.6 ps (Table S3). Therefore, the film preparation procedure results in enhancing the photoconductivity lifetime by at least one order of magnitude compared to the powder sample.

Time-domain THz (THz-TDS) experiments were performed to determine the effect of Cu incorporation on the complex refractive index in the absence of photoexcitation, as described previously.^{47,52-54} Figure 3c shows that the refractive indices of the two materials are essentially identical within error. Furthermore, the complex refractive index is rather temperature independent (Figure S10). These two results imply negligible ground-state doping effects from Cu

incorporation. The enhanced photoconductivity is therefore ascribed to a photodoping effect as further investigated using frequency dependent time-resolved THz spectroscopy (TRTS) at a pump delay of 1.4 ps, as described previously. 32,48,55 The Cu-g-C₃N₄ film sample was sufficiently photoconductive to yield clear TRTS data (Figure 3d). The complex photoconductivity was well-modeled with the Drude-Smith equation as described in the SI and Table S4. In particular, the c-parameter, or persistence of velocity parameter, fit to its limit of -1, suggesting that long-range carrier transport in Cu-g-C₃N₄ is affected by defects or grain boundaries. 30,56,57

The film preparation procedure results in better intra-plane conductivity and/or inter-plane conductivity as a result of better inter-plane contacts. The pXRD results showed closer and more homogeneous stacking of the 2D layers. The fluorescence (Figure S7), XPS (Figures S11-S12) and elemental analysis (Table S5) are suggestive of some electronic and compositional changes due to film preparation, and further studies are required to definitively investigate this effect, particularly with preparations well-suited to anisotropic measurements such as highly-oriented films^{25,58} and/or computational methods⁵⁹ such that intra-plane and inter-plane photoconductivity signals can be separated.

Importantly, a clear increase in photoconductivity due to the presence of Cu ions was demonstrated in this work. These findings are corroborated by the improved photocurrent of Cu-g- C_3N_4 compared to that of g- C_3N_4 in a three-electrode photoelectrochemical cell (Figure S13). The structural characterizations herein demonstrated that Cu-doping resulted in a low-coordinate Cu⁺ species anchored to g- C_3N_4 and gave significantly closer interlayer distances. Cu-doping of g- C_3N_4 also clearly imparts electronic structure changes via UV-Visible and fluorescence quenching. Therefore, we find that Cu-doping plays a two-fold role in enhancing both the intra-plane photoconductivity in g- C_3N_4 via MLCT, which would increase the carrier density compared to

undoped g- C_3N_4 , and inter-plane photoconductivity via closer sheet-to-sheet contact. These findings demonstrate that the photoconductivity of g- C_3N_4 materials is highly tunable in the subnanosecond time regime relevant to light harvesting and photocatalysis and that the improved catalytic efficacy of Cu-doped g- C_3N_4 materials is partly due to the enhanced photoconductivity, in addition to the inclusion of a redox-active metal ion.

In conclusion, Cu^+ doping increased the photoconductivity in g- C_3N_4 as measured by OPTP spectroscopy. X-ray diffraction studies suggested that Cu doping did not significantly alter the bulk structure of g- C_3N_4 and resulted in closer and more homogeneous stacking of the 2D layers. The dopant extended the UV-Visible absorption throughout the visible region of the spectrum due to the presence of an MLCT transition as corroborated by fluorescence quenching. EXAFS analysis showed that the local structure of the dopant is best described as a low-coordinate Cu+species anchored to the 2D sheets of g- C_3N_4 . OPTP experiments using 400 nm excitation showed that the photoconductivity of the Cu-g- C_3N_4 powder decayed within 10 ps and was best described as a heterogeneous process using a stretched exponential decay model. The film preparation utilized yielded a minor photoconductivity component at least one order of magnitude longer than that of the powder sample. These findings demonstrate that rich photoconductivity information accessible by OPTP is present in the ultrafast time regime for g- C_3N_4 and its doped analogues, and that such studies provide important insights to propel further enhancement of g- C_3N_4 toward performing efficient photocatalysis reactions.

ASSOCIATED CONTENT

Supporting Information

The following files are available free of charge.

Supplementary Information (PDF). Experimental, Supplementary photographs, film pXRD figures, EXAFS Figures, undoped g-C₃N₄ OPTP figures, Tauc plots, OPTP instrument schematic, temperature-dependent THz-TDS, photoelectrochemical cell experiments, and XPS figures. Supplementary tables for EXAFS, OPTP, TRTS, and elemental analysis. Atomic cartesian coordinates for EXAFS model.

AUTHOR INFORMATION

Notes

The authors declare no competing financial interests.

ACKNOWLEDGMENT

This work was supported by the U.S. Department of Energy, Office of Science, Office of Basic Energy Sciences, under award DE-FG02-07ER15909, the National Science Foundation under Grant No. 1954453, and from a generous donation from the TomKat Foundation. This research used 6-BM of the National Synchrotron Light Source II, a U.S. Department of Energy (DOE) Office of Science User Facility operated for the DOE Office of Science by Brookhaven National Laboratory under Contract No. DE-SC0012704.

REFERENCES

- (1) Jiang, L.; Yuan, X.; Pan, Y.; Liang, J.; Zeng, G.; Wu, Z.; Wang, H. Doping of Graphitic Carbon Nitride for Photocatalysis: A Review. *Appl. Catal. B* **2017**, *217*, 388-406. DOI: 10.1016/j.apcatb.2017.06.003.
- (2) Zhou, L.; Zhang, H.; Sun, H.; Liu, S.; Tade, M. O.; Wang, S.; Jin, W. Recent Advances in Non-metal Modification of Graphitic Carbon Nitride for Photocatalysis: a Historic Review. *Catal. Sci. Technol.* **2016**, *6*, 7002-7023. DOI: 10.1039/C6CY01195K.
- (3) Wang, X.; Maeda, K.; Thomas, A.; Takanabe, K.; Xin, G.; Carlsson, J. M.; Domen, K.; Antonietti, M. A Metal-free Polymeric Photocatalyst for Hydrogen Production from Water Under Visible Light. *Nature Mater.* **2009**, *8*, 76-80. DOI: 10.1038/nmat2317.
- (4) Yan, S. C.; Li, Z. S.; Zou, Z. G. Photodegradation of Rhodamine B and Methyl Orange over Boron-Doped g-C₃N₄ under Visible Light Irradiation. *Langmuir* **2010**, *26*, 3894-3901. DOI: 10.1021/la904023j.
- (5) Sharma, P.; Sasson, Y. A Photoactive Catalyst Ru–g-C₃N₄ for Hydrogen Transfer Reaction of Aldehydes and Ketones. *Green Chem.* **2017**, *19*, 844-852. DOI: 10.1039/C6GC02949C.
- (6) Li, Y.; Wang, Z.; Xia, T.; Ju, H.; Zhang, K.; Long, R.; Xu, Q.; Wang, C.; Song, L.; Zhu, J.; Jiang, J.; Xiong, Y. Implementing Metal-to-Ligand Charge Transfer in Organic Semiconductor for Improved Visible-Near-Infrared Photocatalysis. *Adv. Mater.* **2016**, 28, 6959-6965. DOI: 10.1002/adma.201601960.
- (7) Zheng, Y.; Lin, L.; Ye, X.; Guo, F.; Wang, X. Helical Graphitic Carbon Nitrides with Photocatalytic and Optical Activities. *Angew. Chem. Int. Ed.* **2014**, *53*, 11926-11930. DOI: 10.1002/anie.201407319.
- (8) Moreira, N. F. F.; Sampaio, M. J.; Ribeiro, A. R.; Silva, C. G.; Faria, J. L.; Silva, A. M. T. Metal-free g-C₃N₄ Photocatalysis of Organic Micropollutants in Urban Wastewater Under Visible Light. *Appl. Catal. B* 2019, 248, 184-192. DOI: 10.1016/j.apcatb.2019.02.001.
- (9) Cui, Y.; Ding, Z.; Liu, P.; Antonietti, M.; Fu, X.; Wang, X. Metal-free Activation of H₂O₂ by g-C₃N₄ Under Visible Light Irradiation for the Degradation of Organic Pollutants. *Phys. Chem. Chem. Phys.* **2012**, *14*, 1455-1462. DOI: 10.1039/C1CP22820J.
- (10) Huang, J.; Ho, W.; Wang, X. Metal-free Disinfection Effects Induced by Graphitic Carbon Nitride Polymers Under Visible Light Illumination. *Chem. Comm.* **2014**, *50*, 4338-4340. DOI: 10.1039/C3CC48374F.
- (11) Su, F.; Mathew, S. C.; Lipner, G.; Fu, X.; Antonietti, M.; Blechert, S.; Wang, X. mpg-C₃N₄-Catalyzed Selective Oxidation of Alcohols Using O₂ and Visible Light. *J. Am. Chem. Soc.* **2010**, *132*, 16299-16301. DOI: 10.1021/ja102866p.
- (12) Geng, P.; Tang, Y.; Pan, G.; Wang, W.; Hu, J.; Cai, Y. A g-C₃N₄-based Heterogeneous Photocatalyst for Visible Light Mediated Aerobic Benzylic C–H Oxygenations. *Green Chem.* **2019**, *21*, 6116-6122. DOI: 10.1039/C9GC02870F.
- (13) Chung, Y. J.; Lee, B. I.; Ko, J. W.; Park, C. B. Photoactive g-C₃N₄ Nanosheets for Light-Induced Suppression of Alzheimer's β-Amyloid Aggregation and Toxicity. *Adv. Healthc. Mater.* 2016, 5, 1560-1565. DOI: 10.1002/adhm.201500964.
- (14) Ran, J.; Ma, T. Y.; Gao, G.; Du, X.-W.; Qiao, S. Z. Porous P-doped Graphitic Carbon Nitride Nanosheets for Synergistically Enhanced Visible-light Photocatalytic H₂ Production. *Energy Environ. Sci.* **2015**, *8*, 3708-3717. DOI: 10.1039/C5EE02650D.
- (15) Thaweesak, S.; Wang, S.; Lyu, M.; Xiao, M.; Peerakiatkhajohn, P.; Wang, L. Boron-doped Graphitic Carbon Nitride Nanosheets for Enhanced Visible Light Photocatalytic Water Splitting. *Dalton Trans.* **2017**, *46*, 10714-10720. DOI: 10.1039/C7DT00933J.

- (16) Faisal, M.; Ismail, A. A.; Harraz, F. A.; Al-Sayari, S. A.; El-Toni, A. M.; Al-Assiri, M. S. Synthesis of Highly Dispersed Silver Doped g-C₃N₄ Nanocomposites with Enhanced Visible-light Photocatalytic Activity. *Mater. Des.* **2016**, *98*, 223-230. DOI: 10.1016/j.matdes.2016.03.019.
- (17) Wang, Z.-T.; Xu, J.-L.; Zhou, H.; Zhang, X. Facile Synthesis of Zn(II)-doped g-C₃N₄ and Their Enhanced Photocatalytic Activity Under Visible Light Irradiation. *Rare Metals* **2019**, 38, 459-467. DOI: 10.1007/s12598-019-01222-5.
- (18) Dong, Q.; Chen, Y.; Wang, L.; Ai, S.; Ding, H. Cu-modified Alkalinized g-C₃N₄ as Photocatalytically Assisted Heterogeneous Fenton-like Catalyst. *Appl. Surf. Sci.* **2017**, 426, 1133-1140. DOI: 10.1016/j.apsusc.2017.07.254.
- (19) Le, S.; Jiang, T.; Zhao, Q.; Liu, X.; Li, Y.; Fang, B.; Gong, M. Cu-doped Mesoporous Graphitic Carbon Nitride for Enhanced Visible-light Driven Photocatalysis. *RSC Adv*. **2016**, *6*, 38811-38819. DOI: 10.1039/C6RA03982K.
- (20) Zhang, T.; Nie, X.; Yu, W.; Guo, X.; Song, C.; Si, R.; Liu, Y.; Zhao, Z. Single Atomic Cu-N₂ Catalytic Sites for Highly Active and Selective Hydroxylation of Benzene to Phenol. *iScience* **2019**, 22, 97-108. DOI: 10.1016/j.isci.2019.11.010.
- (21) Godin, R.; Wang, Y.; Zwijnenburg, M. A.; Tang, J.; Durrant, J. R. Time-Resolved Spectroscopic Investigation of Charge Trapping in Carbon Nitrides Photocatalysts for Hydrogen Generation. *J. Am. Chem. Soc.* **2017**, *139*, 5216-5224. DOI: 10.1021/jacs.7b01547.
- (22) Gao, J.; Zhou, Y.; Li, Z.; Yan, S.; Wang, N.; Zou, Z. High-yield Synthesis of Millimetrelong, Semiconducting Carbon Nitride Nanotubes with Intense Photoluminescence Emission and Reproducible Photoconductivity. *Nanoscale* **2012**, *4*, 3687-3692. DOI: 10.1039/C2NR30777D.
- (23) Aono, M.; Goto, T.; Tamura, N.; Kitazawa, N.; Watanabe, Y. Photoconductivity Study of Amorphous Carbon Nitride Films for Opto-electronics Devices. *Diam. Relat. Mater.* **2011**, 20, 1208-1211. DOI: 10.1016/j.diamond.2011.06.023.
- (24) Zhang, Y.; Thomas, A.; Antonietti, M.; Wang, X. Activation of Carbon Nitride Solids by Protonation: Morphology Changes, Enhanced Ionic Conductivity, and Photoconduction Experiments. *J. Am. Chem. Soc.* **2009**, *131*, 50-51. DOI: 10.1021/ja808329f.
- (25) Miyajima, D.; Arazoe, H.; Kawamoto, M.; Akaike, K.; Koizumi, Y.; Aida, T. G-C₃N₄ Film. U.S. Patent 10,252,253 April 9, 2019
- (26) George, P. A.; Strait, J.; Dawlaty, J.; Shivaraman, S.; Chandrashekhar, M.; Rana, F.; Spencer, M. G. Ultrafast Optical-Pump Terahertz-Probe Spectroscopy of the Carrier Relaxation and Recombination Dynamics in Epitaxial Graphene. *Nano Lett.* **2008**, *8*, 4248-4251. DOI: 10.1021/nl8019399.
- (27) Prechtel, L.; Song, L.; Schuh, D.; Ajayan, P.; Wegscheider, W.; Holleitner, A. W. Timeresolved Ultrafast Photocurrents and Terahertz Generation in Freely Suspended Graphene. *Nature Commun.* **2012**, *3*, 646. DOI: 10.1038/ncomms1656.
- (28) Docherty, C. J.; Parkinson, P.; Joyce, H. J.; Chiu, M.-H.; Chen, C.-H.; Lee, M.-Y.; Li, L.-J.; Herz, L. M.; Johnston, M. B. Ultrafast Transient Terahertz Conductivity of Monolayer MoS₂ and WSe₂ Grown by Chemical Vapor Deposition. *ACS Nano* **2014**, *8*, 11147-11153. DOI: 10.1021/nn5034746.
- (29) Kar, S.; Su, Y.; Nair, R. R.; Sood, A. K. Probing Photoexcited Carriers in a Few-Layer MoS₂ Laminate by Time-Resolved Optical Pump-Terahertz Probe Spectroscopy. *ACS Nano* **2015**, *9*, 12004-12010. DOI: 10.1021/acsnano.5b04804.

- (30) Pattengale, B.; Neu, J.; Ostresh, S.; Hu, G.; Spies, J. A.; Okabe, R.; Brudvig, G. W.; Schmuttenmaer, C. A. Metal–Organic Framework Photoconductivity via Time-Resolved Terahertz Spectroscopy. *J. Am. Chem. Soc.* **2019**, *141*, 9793-9797. DOI: 10.1021/jacs.9b04338.
- (31) Regan, K. P.; Swierk, J. R.; Neu, J.; Schmuttenmaer, C. A. Frequency-Dependent Terahertz Transient Photoconductivity of Mesoporous SnO₂ Films. *J. Phys. Chem. C* **2017**, *121*, 15949-15956. DOI: 10.1021/acs.jpcc.7b02318.
- (32) Beard, M. C.; Turner, G. M.; Schmuttenmaer, C. A. Transient Photoconductivity in GaAs as Measured by Time-resolved Terahertz Spectroscopy. *Phys. Rev. B* **2000**, *62*, 15764-15777. DOI: 10.1103/PhysRevB.62.15764.
- (33) Ulbricht, R.; Hendry, E.; Shan, J.; Heinz, T. F.; Bonn, M. Carrier Dynamics in Semiconductors Studied with Time-resolved Terahertz Spectroscopy. *Rev. Mod. Phys.* **2011**, *83*, 543-586. DOI: 10.1103/RevModPhys.83.543.
- (34) Lotsch, B. V.; Döblinger, M.; Sehnert, J.; Seyfarth, L.; Senker, J.; Oeckler, O.; Schnick, W. Unmasking Melon by a Complementary Approach Employing Electron Diffraction, Solid-State NMR Spectroscopy, and Theoretical Calculations—Structural Characterization of a Carbon Nitride Polymer. *Chem. Eur. J.* **2007**, *13*, 4969-4980. DOI: 10.1002/chem.200601759.
- (35) Fina, F.; Callear, S. K.; Carins, G. M.; Irvine, J. T. S. Structural Investigation of Graphitic Carbon Nitride via XRD and Neutron Diffraction. *Chem. Mater.* **2015**, 27, 2612-2618. DOI: 10.1021/acs.chemmater.5b00411.
- (36) Ito, S.; Chen, P.; Comte, P.; Nazeeruddin, M. K.; Liska, P.; Péchy, P.; Grätzel, M. Fabrication of Screen-printing Pastes from TiO₂ Powders for Dye-sensitised Solar Cells. *Prog. Photovolt.* **2007**, *15*, 603-612. DOI: 10.1002/pip.768.
- (37) Kau, L. S.; Spira-Solomon, D. J.; Penner-Hahn, J. E.; Hodgson, K. O.; Solomon, E. I. Xray Absorption Edge Determination of the Oxidation State and Coordination Number of Copper. Application to the Type 3 Site in Rhus Vernicifera Laccase and its Reaction with Oxygen. *J. Am. Chem. Soc.* **1987**, *109*, 6433-6442. DOI: 10.1021/ja00255a032.
- (38) Wang, J.; Hao, D.; Ye, J.; Umezawa, N. Determination of Crystal Structure of Graphitic Carbon Nitride: Ab Initio Evolutionary Search and Experimental Validation. *Chem. Mater.* **2017**, *29*, 2694-2707. DOI: 10.1021/acs.chemmater.6b02969.
- (39) Hu, K.; Yao, M.; Yang, Z.; Xiao, G.; Zhu, L.; Zhang, H.; Liu, R.; Zou, B.; Liu, B. Pressure tuned photoluminescence and band gap in two-dimensional layered g-C₃N₄: the effect of interlayer interactions. *Nanoscale* **2020**, *12*, 12300-12307. DOI: 10.1039/D0NR01542C.
- (40) Yuan, Y.; Zhang, L.; Xing, J.; Utama, M. I. B.; Lu, X.; Du, K.; Li, Y.; Hu, X.; Wang, S.; Genç, A.; Dunin-Borkowski, R.; Arbiol, J.; Xiong, Q. High-yield synthesis and optical properties of g-C₃N₄. *Nanoscale* **2015**, *7*, 12343-12350. DOI: 10.1039/C5NR02905H.
- (41) Zhang, Y.; Pan, Q.; Chai, G.; Liang, M.; Dong, G.; Zhang, Q.; Qiu, J. Synthesis and luminescence mechanism of multicolor-emitting g-C₃N₄ nanopowders by low temperature thermal condensation of melamine. *Sci. Rep.* **2013**, *3*, 1943. DOI: 10.1038/srep01943.
- (42) Yan, W.; Yan, L.; Jing, C. Impact of doped metals on urea-derived g-C₃N₄ for photocatalytic degradation of antibiotics: Structure, photoactivity and degradation mechanisms. *Appl. Catal. B* **2019**, *244*, 475-485. DOI: 10.1016/j.apcatb.2018.11.069.
- (43) Gao, J.; Wang, Y.; Zhou, S.; Lin, W.; Kong, Y. A Facile One-Step Synthesis of Fe-Doped g-C₃N₄ Nanosheets and Their Improved Visible-Light Photocatalytic Performance. *ChemCatChem* **2017**, *9*, 1708-1715. DOI: 10.1002/cctc.201700492.

- (44) Wang, S.; Shen, C.; Xu, Y.; Zhong, Y.; Wang, C.; Yang, S.; Wang, G. An Improved Metal-to-Ligand Charge Transfer Mechanism for Photocatalytic Hydrogen Evolution. *ChemSusChem* **2019**, *12*, 4221-4228. DOI: 10.1002/cssc.201901609.
- (45) Li, C.; Wang, Y.; Li, C.; Xu, S.; Hou, X.; Wu, P. Simultaneously Broadened Visible Light Absorption and Boosted Intersystem Crossing in Platinum-Doped Graphite Carbon Nitride for Enhanced Photosensitization. *ACS Appl. Mater. Interfaces* **2019**, *11*, 20770-20777. DOI: 10.1021/acsami.9b02767.
- (46) Li, J.; Yan, P.; Li, K.; You, J.; Wang, H.; Cui, W.; Cen, W.; Chu, Y.; Dong, F. Cu supported on polymeric carbon nitride for selective CO₂ reduction into CH₄: a combined kinetics and thermodynamics investigation. *J. Mater. Chem. A* **2019**, *7*, 17014-17021. DOI: 10.1039/C9TA05112K.
- (47) Neu, J.; Schmuttenmaer, C. A. Tutorial: An introduction to terahertz time domain spectroscopy (THz-TDS). *J. Appl. Phys.* **2018**, *124*, 231101. DOI: 10.1063/1.5047659.
- (48) Neu, J.; Ostresh, S.; Regan, K. P.; Spies, J. A.; Schmuttenmaer, C. A. Influence of Dye Sensitizers on Charge Dynamics in SnO₂ Nanoparticles Probed with THz Spectroscopy. *J. Phys. Chem. C* **2020**, *124*, 3482-3488. DOI: 10.1021/acs.jpcc.9b11024.
- (49) Regan, K. P.; Koenigsmann, C.; Sheehan, S. W.; Konezny, S. J.; Schmuttenmaer, C. A. Size-Dependent Ultrafast Charge Carrier Dynamics of WO₃ for Photoelectrochemical Cells. *J. Phys. Chem. C* **2016**, *120*, 14926-14933. DOI: 10.1021/acs.jpcc.6b04390.
- (50) Turner, G. M.; Beard, M. C.; Schmuttenmaer, C. A. Carrier Localization and Cooling in Dye-Sensitized Nanocrystalline Titanium Dioxide. *J. Phys. Chem. B* **2002**, *106*, 11716-11719. DOI: 10.1021/jp025844e.
- (51) Elton, D. C. Stretched Exponential Relaxation. arXiv 2018, 1808.00881.
- (52) Neu, J.; Stone, E. A.; Spies, J. A.; Storch, G.; Hatano, A. S.; Mercado, B. Q.; Miller, S. J.; Schmuttenmaer, C. A. Terahertz Spectroscopy of Tetrameric Peptides. *J. Phys. Chem. Lett.* **2019**, *10*, 2624-2628. DOI: 10.1021/acs.jpclett.9b01091.
- (53) Neu, J.; Nikonow, H.; Schmuttenmaer, C. A. Terahertz Spectroscopy and Density Functional Theory Calculations of dl-Norleucine and dl-Methionine. *J. Phys. Chem. A* **2018**, *122*, 5978-5982. DOI: 10.1021/acs.jpca.8b04978.
- (54) Neu, J.; Nemes, C. T.; Regan, K. P.; Williams, M. R. C.; Schmuttenmaer, C. A. Exploring the solid state phase transition in dl-norvaline with terahertz spectroscopy. *Phys. Chem. Chem. Phys.* **2018**, *20*, 276-283. DOI: 10.1039/C7CP05479C.
- (55) Neu, J.; Regan, K. P.; Swierk, J. R.; Schmuttenmaer, C. A. Applicability of the thin-film approximation in terahertz photoconductivity measurements. *Appl. Phys. Lett.* **2018**, *113*, 233901. DOI: 10.1063/1.5052232.
- (56) Smith, N. V. Classical generalization of the Drude formula for the optical conductivity. *Phys. Rev. B* **2001**, *64*, 155106. DOI: 10.1103/PhysRevB.64.155106.
- (57) Cocker, T. L.; Baillie, D.; Buruma, M.; Titova, L. V.; Sydora, R. D.; Marsiglio, F.; Hegmann, F. A. Microscopic origin of the Drude-Smith model. *Phys. Rev. B* **2017**, *96*, 205439. DOI: 10.1103/PhysRevB.96.205439.
- (58) Villalobos, L. F.; Vahdat, M. T.; Dakhchoune, M.; Nadizadeh, Z.; Mensi, M.; Oveisi, E.; Campi, D.; Marzari, N.; Agrawal, K. V. Large-scale Synthesis of Crystalline g-C₃N₄ Nanosheets and High-temperature H₂ Sieving from Assembled Films. *Science Adv.* **2020**, *6*, eaay9851. DOI: 10.1126/sciadv.aay9851.

(59) Ma, X.; Lv, Y.; Xu, J.; Liu, Y.; Zhang, R.; Zhu, Y. A Strategy of Enhancing the Photoactivity of g-C₃N₄ via Doping of Nonmetal Elements: A First-Principles Study. *J. Phys. Chem. C* **2012**, *116*, 23485-23493. DOI: 10.1021/jp308334x.